

See discussions, stats, and author profiles for this publication at: <https://www.researchgate.net/publication/231698212>

# Dual-Axis Electron Tomography for Three-Dimensional Observations of Polymeric Nanostructures

ARTICLE *in* MACROMOLECULES · OCTOBER 2005

Impact Factor: 5.8 · DOI: 10.1021/ma051705u

---

CITATIONS

49

---

READS

36

3 AUTHORS, INCLUDING:



**Toshio Nishi**

Tokyo Institute of Technology

216 PUBLICATIONS 4,879 CITATIONS

SEE PROFILE



**Hiroshi Jinnai**

Tohoku University

234 PUBLICATIONS 4,241 CITATIONS

SEE PROFILE

# Dual-Axis Electron Tomography for Three-Dimensional Observations of Polymeric Nanostructures

Hidekazu Sugimori,<sup>†</sup> Toshio Nishi,<sup>‡</sup> and Hiroshi Jinnai<sup>\*,†</sup>

Department of Polymer Science and Engineering, Kyoto Institute of Technology, Matsugasaki, Kyoto 606-8585, Japan, and Department of Organic and Polymeric Materials, School of Science and Engineering, Tokyo Institute of Technology, 2-12-1, Ohokayama, Meguro-ku, Tokyo 152-8552, Japan

Received August 1, 2005; Revised Manuscript Received September 20, 2005

**ABSTRACT:** Transmission electron microtomography (TEMT) has proven to be useful for investigating three-dimensional (3D) nanostructures in polymeric systems. However, the conventional TEMT that uses a tilt series around an axis occasionally fails to reconstruct nanostructures, especially when the nanostructure is highly anisotropic. Namely, if a certain geometrical relationship between orientation of the nanostructure and the tilt axis is fulfilled, the nanostructure does not appear in the 3D reconstruction. This problem can be solved by tilting the specimen around two (orthogonal) tilt axes and combining the resulting two 3D reconstructions after precise alignment between them. The strategy, called “dual-axis tomography”, is used to observe one of the commonly observed anisotropic polymer nanostructures, cylindrical morphology, of poly(styrene-*block*-isoprene) block copolymer. It was experimentally observed that the cylindrical nanodomains that were “missing” in one of the two tomograms were complementary reconstructed in the other tomogram obtained from the tilt series using the orthogonal tilt axis to the first data set. Subsequently, the two 3D reconstructions were combined to generate a new 3D reconstruction, in which the cylinders at any orientation were successfully imaged with improved image quality. Although the single-axis tomography gave always lower volume fraction of the cylindrical microdomains than the predicted one calculated on the basis of known molecular composition, an excellent agreement was obtained between the two in the dual-axis tomography. In addition, 3D images taken by the TEMT were shown to be quite effective to determine the nanostructure, i.e., cylindrical structure, which otherwise could be assigned to be lamellar nanostructure by other (surface) observation technique such as AFM or SEM.

## I. Introduction

With the rapid advances in nanotechnology, structural scales of many functional and engineering materials, e.g., microelectronic devices,<sup>1</sup> semiconductors,<sup>2</sup> high-strength superalloys, and various composite materials, have become ever smaller. A block copolymer, one of the macromolecular systems, is of current interest in nanotechnology.<sup>3</sup> It consists of dissimilar (A and B) sequences and exhibits highly periodic and often very complex nanostructures.<sup>4</sup> With the basic knowledge of a relationship between the molecular architecture and resulting three-dimensional (3D) structure, morphological design of nanostructures may become more practical, giving greater flexibility in various applications of the block copolymers in nanometer scale, e.g., a nanocrystal flash memory device,<sup>5</sup> a nanoscale porous material that can be used for catalyst and membrane,<sup>6</sup> low dielectric constant material,<sup>7</sup> etc.

To elucidate such an architecture–morphology relation, there is a growing need for a technique to examine the morphology of a few hundred nanometers in dimension with 1 nm spatial resolution in all three dimensions to gain a full picture of the structure. Thus, transmission electron microtomography (TEMT)<sup>8</sup> is an ideal tool to characterize the block copolymer nanostructures, and as such, it has proven useful for providing high-resolution 3D information about a variety of polymeric structures, e.g., block copolymer nanoscale microphase-

separated structures,<sup>9–15</sup> polymer/clay nanocomposite materials,<sup>16</sup> carbon black/natural rubber composite,<sup>17</sup> etc. Some of these studies provided not only 3D pictures but also quantitative structural analysis, through which the packing frustration of polymer chains in the block copolymer nanostructures was discussed.<sup>11</sup>

In the TEMT experiments, a series of tilted transmitted images (projections) are taken by transmission electron microscopy (TEM) and is used to reconstruct tomograms on the basis of computerized tomography (CT). The tomograms are then stacked to generate a 3D reconstructed image (“3D reconstruction”). There is an intrinsic limitation of angular range for a tilting experiment available with TEM,<sup>18</sup> which results in a “missing wedge” of information in Fourier space (see section II for details). Because of the missing wedge, resolution along the direction parallel to the optical axis of the microscope (the dimension perpendicular to the plane of the specimen), i.e., *z*-direction, is reduced compared to that in the specimen plane.<sup>19</sup> In addition to this primary effect, a less appreciated but probably critical effect of the missing wedge is that the resolution for elongated features in the plane of the specimen depends strongly on their angle relative to the tilt axis. Although the cylindrical and lamellar morphologies of the block copolymers could be influenced by the latter effect in the TEMT observations, none of the previous studies dealing with such anisotropic nanostructures<sup>9</sup> considered the effect.

In the present paper, we apply the dual-axis tomography to a cylindrical nanostructure of a diblock copolymer in order to examine the effectiveness of the method in the 3D observation of such highly anisotropic

<sup>†</sup> Kyoto Institute of Technology.

<sup>‡</sup> Tokyo Institute of Technology.

\* To whom correspondence should be addressed: e-mail hjinnai@kit.ac.jp.

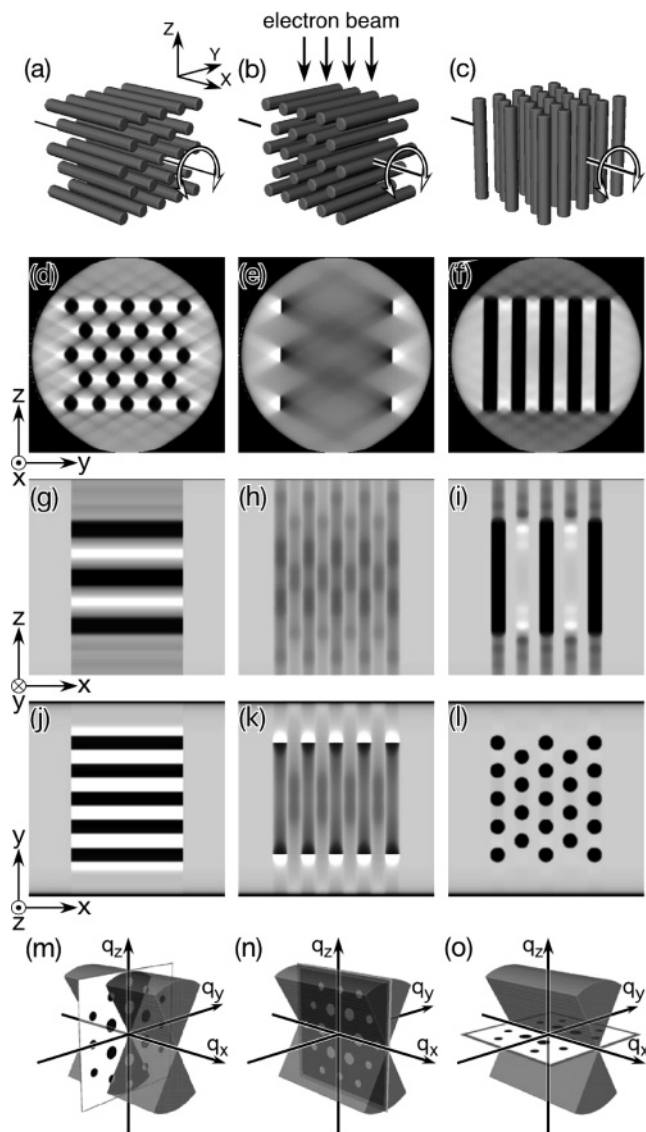


**Figure 1.** Demonstration of the effect of geometrical relationship between direction of tilt axis and orientation of cylindrical nanodomains on 3D reconstruction. There are three types of geometrical relationship. Each column shows a model, three cross sections of 3D reconstruction, and a “missing wedge” in Fourier space (shown by gray volume), from top to the bottom. The cylindrical nanodomains rotate around the tilt axis from  $-60^\circ$  to  $60^\circ$  with  $1^\circ$  increment. Tilt axis is always along the  $x$ -direction. Electron beam comes from top (from the  $z$ -direction). An  $x$ - $z$  cross section is a tomogram where the filtered back projection (FBP) is carried out. In the bottom-most row, diffraction patterns from the infinitely long cylinders are shown together with the missing wedge. Since the missing wedge is the volume in Fourier space where no projections can be sampled, diffraction spots within this wedge cannot contribute to the resulting 3D reconstruction.

polymeric nanostructure. Improvement of image quality over the conventional single-axis tomography will be discussed.

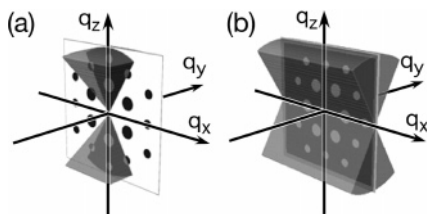
## II. Theoretical Background

Figure 1 shows a simulation of the single-axis TEMT for cylindrical morphologies. As shown in Figure 1a–c, three different geometries in terms of the tilt axis and orientation of the cylinders were simulated. In these three figures, the hexagonally packed cylinders orient toward three different directions while the tilt axis is fixed to the  $x$ -direction. In the same manner as TEMT

experiments, the cylinders were tilted around the tilt axis typically from  $-60^\circ$  to  $60^\circ$  with an increment of  $1^\circ$ , from which the filtered back-projection method<sup>20,21</sup> was used to obtain tomograms. Figure 1d–l displays cross-sectional images of the 3D reconstruction. In the  $y$ - $z$  plane, the cross sections corresponding to models (a) and (c) were properly reproduced, while those of models (b) and (e) were poorly reconstructed; The horizontal stripes should be observed. Figure 1g–i and Figure 1j–l show respectively  $x$ - $z$  and  $x$ - $y$  planes. Although the cross sections relevant to models (a) and (c) were reasonably obtained, again, the cross sections corresponding to model (b) (see Figure 1h,k) were not correctly reconstructed. In fact, judging only from the cross-sectional images obtained from model (b), i.e., Figure 1e,h,k, one could misidentify the 3D structure with the lamellar morphology whose lamellar normal aligned with the  $x$ -axis. Thus, if the orientation of the cylindrical nanodomains geometrically satisfies the relation with the tilt axis as shown in Figure 1b, it is quite likely that the cylinders do not appear in the 3D reconstruction.

This problem can be understood by considering a relationship between a projection in real space and Fourier space. The “central slice theorem” upon which the CT relies states that the Fourier transformation of a projection at a given angle is a central section at the same angle through the Fourier transform of that object.<sup>20,22</sup> Thus, if a series of projections are acquired at different tilt angles, each projection will equate to part of an object’s Fourier transform. Therefore, in principle, tomographic reconstruction is possible from an inverse Fourier transform of the superposition of a set of Fourier transformed projections. If some projections are missing from an angular range as in the TEMT, which is brought about by a limit on the maximum tilt angle, then the Fourier space is under-sampled in those directions. The unsampled volume in the Fourier space becomes wedge shaped and thus is called the “missing wedge”. As a consequence of this unsampled volume, the back transform, the tomogram of the object, will be degraded. Figure 1m–o demonstrates the missing wedge in Fourier space (translucent gray volume) and “diffraction pattern” of the cylindrical nanodomains relevant to the geometries shown in Figure 1a–c, respectively. Although the tilt axis lies along the  $x$ -direction in all models, the orientations of the cylinders are different, and hence the diffraction spots of the cylindrical nanodomains appear differently. In the case of Figure 1m,o, part of and all of the diffraction spots are outside the missing wedge, and thus it is feasible to obtain the reasonable 3D reconstructions. In fact, the image quality of 3D reconstruction of model (c) appears to be the best among the three geometries (see Figure 1l for example) because all diffraction spots can be sampled irrespective of the existence of the missing wedge. On the other hand, all the diffraction spots are inside the missing wedge in Figure 1h, resulting in the insufficient 3D reconstruction as described above.

Let us now consider how to solve the problem associated with the missing wedge. As shown in Figure 1, whether a diffraction pattern of a structure in Fourier space (and hence orientation of the structure in real space) is inside the missing wedge or not is the crucial issue. Therefore, one of the most effective ways to improve image quality of the resulting 3D reconstruction is to minimize the volume of the missing wedge to



**Figure 2.** Comparison of missing volume in Fourier space between (a) dual-axis tomography and (b) single-axis tomography. Directions of tilt axes in the dual-axis tomography are along  $q_x$  and  $q_y$  axes. In single-axis tomography, tilt axis is along  $q_x$  axis. Hexagonally packed infinitely long cylindrical morphology aligned along  $y$ -axis as shown in Figure 1b gives diffraction pattern only in the  $q_x$ - $q_z$  plane. Some of the diffraction spots are outside the “missing pyramid”, and hence the cylinders can be reconstructed in dual-axis tomography (a), while all diffraction spots are inside the “missing wedge” in single-axis tomography (b).

a maximum extent. Although one normally achieves this goal by tilting the specimen to the highest tilt angle possible, this strategy would not help much, especially in the case of the 3D observation of cylindrical morphology as demonstrated in Figure 1b. Another strategy is to have another tilt axis in addition to the first one. Figure 2 demonstrates such “dual-axis tomography”: In Figure 2a the unsampled volume of the dual-axis tomography is shown. Note that the additional tilt axis is along the  $y$ -direction, while the first one is along the  $x$ -direction. Compared with the missing wedge shown in Figure 2b (that is the reproduction of Figure 1n), the unsampled volume in the dual-axis tomography, called the “missing pyramid”, becomes considerably smaller than the missing wedge. A part of the diffraction spots of the cylindrical nanodomains is now outside the missing pyramid, indicating that the cylinders would be reconstructed. Penczek et al.<sup>23</sup> pioneered the dual-axis tomography for thick biological sections, followed by Mastronarde.<sup>24</sup>

### III. Experimental Section

**A. Materials.** A poly(styrene-*block*-isoprene) (SI) block copolymer was purchased from Polymer Source Inc., Canada. The number-averaged molecular weight and polydispersity index are  $M_n = 5.1 \times 10^4$  and  $M_w/M_n = 1.06$ . The isoprene volume fraction,  $f_i$ , was calculated to be 0.22 according to the mass densities reported for polystyrene (S) and polyisoprene (I) (0.913 g/cm<sup>3</sup> for I and 1.04 g/cm<sup>3</sup> for S).

**B. Specimens.** A mica substrate was cleaved and then coated with carbon by vacuum deposition in advance. A specimen film was prepared by spin-coating from 5 wt % toluene solution of the SI copolymer onto the mica substrate. The copolymer film on the substrate was further annealed at 140 °C for a week under vacuum. The annealed thin film was floated off the mica substrate and was picked up onto Cu mesh grid. The film was stained with OsO<sub>4</sub> vapor for 5 min. Prior to the TEM and transmission electron microscopy (TEM) experiments, gold particles of 10 nm diameter were deposited from aqueous suspension. Note here that the gold particles were placed on both sides of the section.

**C. Dual-Axis Transmission Electron Microtomography.** The TEM and TEMT experiments were carried out on a JEM-2200FS (JEOL Ltd., Japan) operated at 200 kV. The digital data of the transmitted images were collected with a slow-scan CCD camera (Gatan USC1000, Gatan Inc.). Two sets of tilt series were taken at the same area of the specimen. A projection at each tilt angle was acquired with frame size of 1024 by 1024 pixels. To obtain achromatic projections, only the transmitted and elastically scattered electrons (electron energy loss:  $0 \pm 30$  eV) were selected by an energy filter installed in a JEM-2200FS ( $\Omega$  filter, JEOL Ltd., Japan). The

first tilt series was taken over the tilt angle from  $-60^\circ$  to  $+66^\circ$  with  $1^\circ$  increment. After the first series were completed, the Cu mesh grid was rotated manually by ca.  $90^\circ$ , and the second tilt series was acquired again over the tilt angles ranging from  $-70^\circ$  to  $+65^\circ$  with  $1^\circ$  increment. The pixel size was 1.9 nm.

Prior to computing a 3D reconstruction, an alignment of the tilt series was first necessary because there is an uncontrolled and magnification-dependent rotation of the projection by the electron optics within the microscope. This alignment also determines the tilt axis within the TEM micrographs and corrects any miscalibration in the goniometer stage. Each tilt series was aligned separately using 10 nm gold particles placed on the section. An area common to each projection in the tilt series was utilized to perform the alignment by tracing the motions of several fiducial points in the area.<sup>18</sup> Note that the mean alignment error,<sup>25</sup> averaged over all of the fiducial markers used in the alignment, was less than the pixel resolution regardless of the tilt angles. The tilt series after the alignment were subsequently reconstructed by the filtered back-projection (FBP) algorithm.<sup>26</sup> Hereafter, we call the 3D reconstruction obtained from the first and second tilt series “reconstruction 1” and “reconstruction 2”, respectively.

**D. Combining 3D Reconstructions from the Two Tilt Series.** As described in the previous section, the alignment by the fiducial marker method and the following reconstruction results in two sets of 3D reconstructions, i.e., reconstruction 1 and 2, and a pair of 3D coordinates (one from each tilt series) for the fiducial markers on the specimen. Dual-axis TEMT follows two more steps: (i) making two reconstructions at the same position and orientation and (ii) synthesis of the reconstructions in Fourier space. The coordinates in reconstruction 2,  $\mathbf{x}_2$ , can be related to those in reconstruction 1,  $\mathbf{x}_1$ , by the following equation:

$$\mathbf{x}_1 = \mathbf{A}\mathbf{x}_2 + \mathbf{b} \quad (1)$$

where  $\mathbf{A}$  is a transformation matrix

$$\mathbf{A} = \begin{pmatrix} a_{11} & a_{12} & a_{13} \\ a_{21} & a_{22} & a_{23} \\ a_{31} & a_{32} & a_{33} \end{pmatrix} \quad (2)$$

and  $\mathbf{b}$  is a translation vector:

$$\mathbf{b} = \begin{pmatrix} b_1 \\ b_2 \\ b_3 \end{pmatrix} \quad (3)$$

$\mathbf{b}$  adjusts the position of reconstruction 2, and  $\mathbf{A}$  adjusts the orientation (3 degrees of freedom). The transformation matrix  $\mathbf{A}$  also includes the operation for scaling and skewing. Scaling operation (3 degrees of freedom) corrects the magnification change of the TEMT image due to the focus change of TEM. Skewing operation (3 degrees of freedom) corrects the slight astigmatism in the TEMT image. It appears that both scaling and skewing operations are preferable to achieve high precision in adjusting reconstruction 2 onto reconstruction 1. The precision of adjustment directly affects the resolution of the resulting dual-axis TEMT image. An error of 1 pixel in the adjustment easily leads to loss of 1 pixel in resolution in the combined TEMT 3D reconstruction.

Let the coordinate of the  $n$ th gold marker in reconstruction 1 to be  $\mathbf{p}_{n,1}$  and that of the relevant marker in reconstruction 2 to be  $\mathbf{p}_{n,2}$ . The  $\mathbf{p}_{n,2}$  is transferred by eq 1 into  $\mathbf{p}'_{n,2}$ , which should be equal to  $\mathbf{p}_{n,1}$ . Hence

$$|\mathbf{p}_{n,1} - \mathbf{p}'_{n,2}| = 0 \quad (4)$$

The parameters in  $\mathbf{A}$  and  $\mathbf{b}$  can be determined by the least-squares fitting to achieve the condition described in eq 4. Note that the markers should be located on both sides or inside the specimen in order to determine 12 parameters in  $\mathbf{A}$  and  $\mathbf{b}$ .

If the markers are only on one side of specimen,  $z$ -coordinates of the markers are not available in the fitting



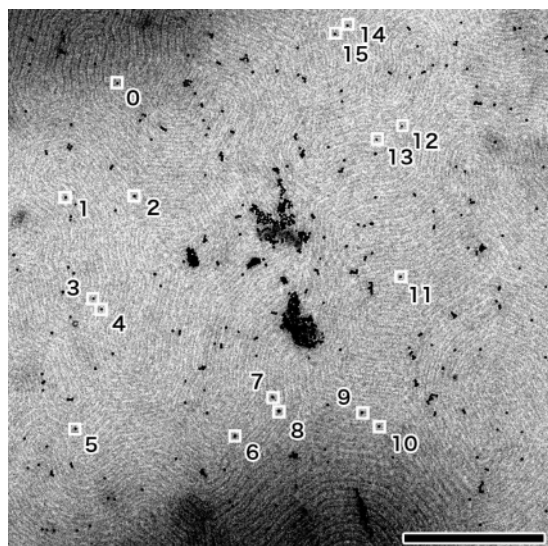


**Figure 3.** TEM micrograph of SI block copolymer. Dark phases show  $\text{OsO}_4$ -stained PI nanodomains. Small black dots are gold nanoparticles. The gold nanoparticles surrounded by white rectangles were used for aligning the tilt series and for combining two 3D reconstructions shown in Figure 4 with orthogonal axes. 16 particles (numbered) were used for these purpose. The number of gold nanoparticles here is the same as that in Figure 5. Bar shows 500 nm.

procedure, so that  $a_{31}$ ,  $a_{32}$ , and  $a_{33}$  of  $\mathbf{A}$ , which are the coefficients for the  $z$ -coordinates of markers in eq 1, cannot be determined. Alternatively,  $a_{31}$ ,  $a_{32}$ , and  $a_{33}$  may be estimated by the following equation:

$$\begin{pmatrix} a_{31} & a_{32} & a_{33} \end{pmatrix} = \frac{\begin{pmatrix} a_{11} & a_{12} & a_{13} \end{pmatrix}}{\begin{vmatrix} a_{11} & a_{12} & a_{13} \\ a_{21} & a_{22} & a_{23} \end{vmatrix}} \times \begin{pmatrix} a_{21} & a_{22} & a_{23} \end{pmatrix} \quad (5)$$

Equation 5 assumes no distortion and no scaling on the  $z$ -direction. Incorporating eq 5 into the fitting condition described by eq 4, the remaining nine parameters can be determined from the coordinates of the markers only on one side of the specimen.

Now that the coordinate of reconstruction 2 is transformed according to eq 1, the two 3D reconstructions can be synthesized in Fourier space<sup>24</sup> (not in real space<sup>23</sup>). The Fourier transform of the tomogram is

$$F_j(\mathbf{q}_1) = \int f_j(\mathbf{x}_1) e^{-i\mathbf{q}_1 \cdot \mathbf{x}_1} d\mathbf{x}_1 \quad (6)$$

where  $\mathbf{q}_1$ ,  $F_j$ , and  $f_j$  are respectively coordinates in the Fourier space, Fourier spectrum, and the real-space image of the 3D reconstruction  $j$  ( $j = 1, 2$ ). The combination of the two 3D reconstructions in Fourier space is carried out in the following way. If  $\mathbf{q}_1$  is neither inside the missing wedge of  $F_1$  nor inside the missing wedge of  $F_2$ , the synthesized Fourier spectrum,  $F(\mathbf{q}_1)$ , is an average of them, i.e.,  $F(\mathbf{q}_1) = (F_1(\mathbf{q}_1) + F_2(\mathbf{q}_1))/2$ . In case  $\mathbf{q}_1$  is inside the missing pyramid as shown in Figure 2b, no data are available and hence  $F(\mathbf{q}_1) = 0$ . If  $\mathbf{q}_1$  locates inside the missing wedge of reconstruction 1 but not inside the missing wedge of reconstruction 2,  $F(\mathbf{q}_1) = F_2(\mathbf{q}_1)$  and vice versa. Although the position of the missing wedge of reconstruction 2 in  $\mathbf{q}_1$  coordinate is not obvious due to the rotation and/or distortion during the coordinate transformation, it is relatively easy to find the coordinate of the missing wedge in  $\mathbf{q}_2$  space. By using a simple relationship  $\mathbf{q}_2 \equiv \mathbf{q}_1/\mathbf{A}$  (see Appendix for details),  $\mathbf{q}_2$  can be easily translated to  $\mathbf{q}_1$ , and hence one can find the position of the missing wedge of reconstruction 2 in  $\mathbf{q}_1$  space.

#### IV. Results and Discussion

Figure 3 displays a TEM micrograph of the SI block copolymer. Since the thickness of the section was rather

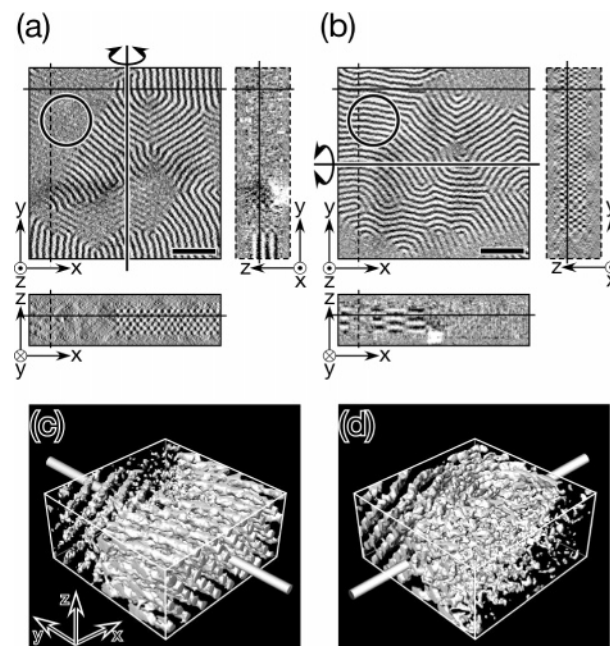


**Figure 4.** Orthogonal cross-sectional views of (a) reconstruction 1 and (b) reconstruction 2. Tilt axes lie along (a)  $y$ - and (b)  $x$ -direction, respectively. In (a) and (b), as indicated by the circles, some cylindrical nanodomains were not reproduced in (a) but nicely reconstructed in (b) and vice versa. Solid and dashed lines in cross sections represent positions where each slice was cut in 3D reconstructed data. (c) and (d) show surface-rendered 3D images, where PS region has been made transparent. Tilt axes are indicated by solid rods. Scale bar in (a) and (b) shows 200 nm. Box size of the 3D image is 250 nm  $\times$  250 nm  $\times$  115 nm.

thick (ca. 160 nm), the nanostructure overlapped along the  $z$ -direction, and hence the detailed features of the nanostructure were not clearly identified. According to the volume fraction of the isoprene in the SI block copolymer, the nanostructure should be cylinders. Small dots in the figure were gold nanoparticles used for aligning the tilt series and also for combining the two 3D reconstructions having orthogonal tilt axes. In the middle of the picture, there were large aggregates of the gold particles, which were used to find the same field of view after rotating the section by ca. 90°.

The 3D reconstructions of the two tilt series are shown in Figure 4. Parts a and b of Figure 4 display respectively orthogonal views of reconstruction 1 and reconstruction 2 whose tilt axes were along  $y$ - and  $x$ -directions. The solid and dashed lines in each cross-sectional slice represent positions of the other two orthogonal slices. The thickness of the three cross sections in Figure 4a,b was equal to the edge length of a voxel, i.e., 1.9 nm. Thus, in contrast to the conventional TEM micrograph shown in Figure 3, the images were outstandingly clear due to essentially no overlap of the nanostructure. The cross-sectional slice will be called the “digital slice” throughout this paper. Moreover, one of the biggest advantages of TEMT is that it obtains truly 3D information on intact block copolymer morphology by digital sectioning, instead of physically cutting the materials into slices.

The two 3D reconstructions show exactly the same volume of the section except for the direction of the tilt axis. It is now obvious that the SI block copolymer exhibited PI cylindrical morphology. The cylinders lied parallel to the film surface. Since the alignment of the tilt series was precisely done, the cross sections in the

$x$ - $z$  plane in Figure 4a and the  $y$ - $z$  plane in Figure 4b were clearly observed, from which the thickness of the film was measured to be ca. 160 nm. It was found that there were six layers of cylindrical nanodomains in the film as observed from the  $x$ - $z$  plane in Figure 4a and the  $y$ - $z$  plane in Figure 4b.

It is quite intriguing that some parts of the 3D reconstruction either in Figure 4a or in Figure 4b were not properly reconstructed: For example, the horizontally oriented cylinders shown by a circle in the  $x$ - $y$  plane of Figure 4a were only vaguely visible, while they were clearly visible in the  $x$ - $y$  plane of Figure 4b (corresponding part was also indicated by a circle). As described earlier in section II, the cylinders in this area fulfilled the geometrical relation with the tilt axis as shown in Figure 1b, and hence they would not properly be reconstructed. On the other hand, since the same cylinders were parallel to the tilt axis ( $x$ -axis) in reconstruction 2, corresponding to the situation shown in Figure 1a, they were successfully reconstructed (Figure 4b). These results demonstrate that the change in relative angle of the cylinders with respect to the tilt axis by the rotation of the section made it possible to reconstruct the nanodomains that did not appear under a certain experimental setup.

The interface between the PI and PS nanodomains were found by binarizing the morphologies in the  $x$ - $y$  plane and was reconstructed according to the marching cubes algorithm (MCA).<sup>27</sup> Parts c and d of Figure 4 show surface-rendered 3D images of the SI block copolymer corresponding to reconstruction 1 and reconstruction 2, respectively. The tilt axes are indicated as translucent rods in the figures. Again, it is clearly observed that some cylindrical nanodomains were missing. The volume fraction of the PI nanodomains evaluated from parts c and d of Figure 4 were respectively 0.16 and 0.15, in contradiction to the known composition of the copolymer ( $f_i = 0.22$ ).

Let us now discuss a combination of the 3D reconstructions from two tilt series to generate a new 3D reconstruction according to the protocol described earlier in section III.D. Figure 5 demonstrates the accuracy in the combination, in which positions of the 16 gold nanoparticles used in the combination procedure are shown. The gray stripes in the  $x$ - $z$  and  $y$ - $z$  planes indicate the section of the SI block copolymer. The filled circles represent the positions of the 16 gold particles in reconstruction 1. Following the procedures described in section III.D, the coordinate of reconstruction 2 was translated according to eq 1. The open squares in Figure 5 show the positions of the gold particles of reconstruction 2 after the coordinate transformation. The positions of the gold particles agreed quite well between the two reconstructions, demonstrating that the protocol in section III.D went well. A mean positioning error averaged over the 16 markers in the combination process was ca. 0.66 pixel.

Since the coordinate transformation has been successfully carried out, let us now combine the two 3D reconstructions. Parts a and b of Figure 6 display the digital slices of reconstruction 1 and reconstruction 2, respectively. The tilt axes were directions along the  $y$ - and  $x$ -axes, respectively. Some parts of the cylindrical nanodomains were missing as described earlier (see Figure 4 for details). The two 3D reconstructions were combined into a new 3D reconstruction in real space (Figure 6c) and in Fourier space (Figure 6d). Figure 6c,d

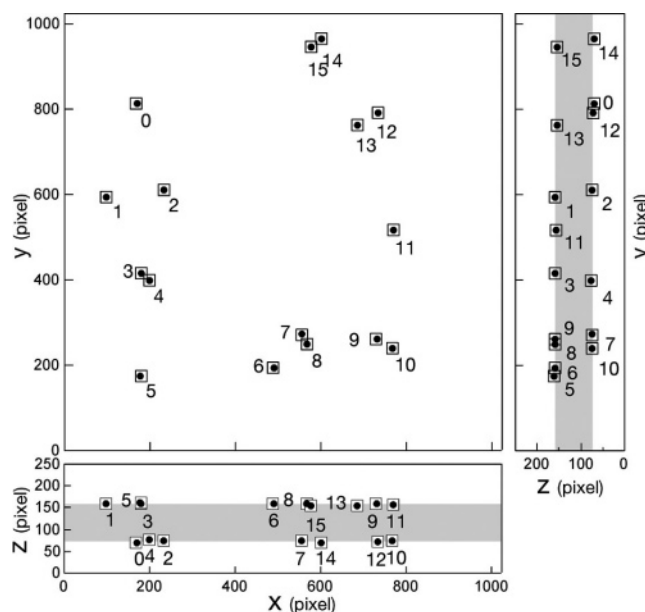


**Figure 5.** Orthogonal cross-sectional views demonstrating precision of the combination of the two 3D reconstruction. 16 gold nanoparticles placed both sides of the section used as markers for combination are shown. Filled circles represent positions of the gold particles in reconstruction 1, while open squares show positions of the markers after coordinate transformation as described in section III.D. Gray stripes indicate the specimen, from which thickness of the section was estimated.

shows the digital slices of the combined 3D reconstruction at the same field of view and depth as those shown in Figure 6a,b. In both digital slices, cylindrical nanodomains at all orientation were successfully reproduced. However, there observed a certain difference in the image quality between the two: the image contrast of digital slice shown in Figure 6d was more uniform than that in Figure 6c.

The difference of image quality came from the combination protocols. In Figure 6c, the digital slices having orthogonal tilt axes at the same depth position in the specimen were simply averaged to obtain the combined slice. If the nanostructures appeared only in one of the two 3D reconstructions, the averaging was carried out between the cylindrical nanostructures in one of the two 3D reconstructions and the noise in the other 3D reconstruction. Consequently, the signal-to-noise ratio (S/N) became worse than the original cylindrical domains. For example, the areas of the upper left corner in Figure 6a,b (marked by circles) were averaged to generate the same area in Figure 6c, the image quality of which was worse than the original (Figure 6a). On the other hand, if the nanostructures appeared in Figure 6a,b (such as the central part of the digital slices), they were averaged, and hence the S/N at this part was substantially increased, giving rise to superior image quality to the original images. Thus, the nonuniform image quality was observed. On the other hand, the digital slice shown in Figure 6d was synthesized in Fourier space as detailed in section III.D. The synthesized Fourier transform was inversely Fourier transformed in order to obtain tomographic reconstruction. The digital slice displayed in Figure 6d showed a distinct image over the whole field of view.

The histograms of the digital slices,  $H$ , obtained from the single-axis tomography were broad and single-peaked (see the histograms underneath Figure 6a,b).



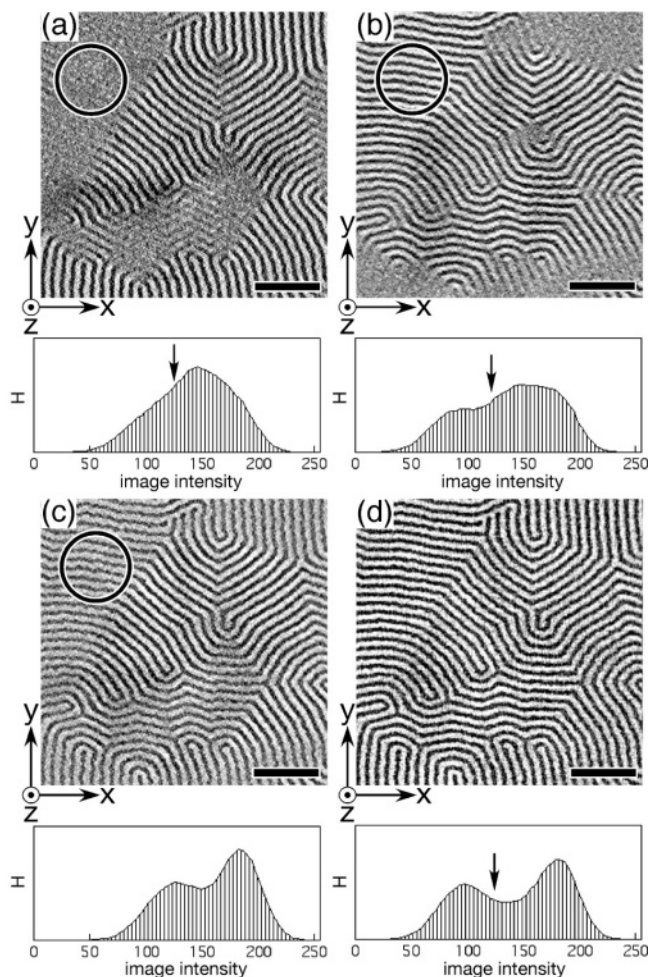


**Figure 6.** Digital slices of single-axis and dual-axis tomography in the same area of 3D reconstructed data: (a) reconstruction 1 and (b) reconstruction 2. Directions of the tilt axes of these 3D reconstruction are  $y$ - and  $x$ -directions, respectively. (c) and (d) show the digital slices at the relevant field of views obtained by combining the two 3D reconstructions in (c) real space and (d) Fourier space. Histogram of each digital slice is shown underneath the corresponding image. Bar shows 200 nm.

In contrast, the averaged digital slices in real space exhibited double-peaked histograms. The histogram of the combined digital image in Fourier space (Figure 6d) also had two peaks but more clearly separated, and its pixel intensities were more widely spread than those of the digital slice averaged in real space, indicating better image contrast.

Orthogonal views of the combined 3D reconstruction (in Fourier space) are displayed in Figure 7a together with a corresponding surface-rendered 3D image in Figure 7b. The threshold used for binarization of the digital slice, e.g., the one shown in Figure 6d, was indicated by an arrow in the histogram in Figure 6d. Since the positions of the orthogonal views in Figure 7a are exactly the same as those in Figure 4a,b, it is now obvious how much the dual-axis tomography can improve the single-axis 3D reconstructions: not only in the plane of the specimen ( $x$ - $y$  plane) but also in the cross-sectional planes, i.e.,  $x$ - $z$  and  $y$ - $z$  planes, cylindrical nanodomains were visible regardless of their orientations. The volume fraction of the PI domains were evaluated from the surface-rendered image:  $f_1$  was ca. 0.22, in excellent agreement with the known composition of the copolymer. This result indicates that only

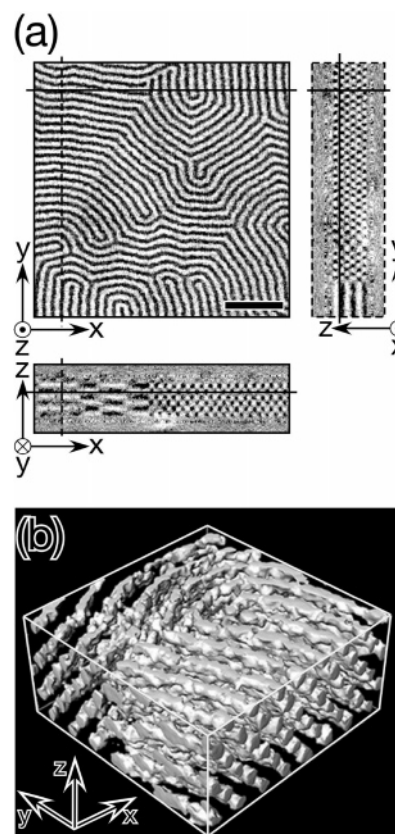


**Figure 7.** (a) Orthogonal cross-sectional views of 3D reconstructions obtained from dual-axis tomography. Positions of the cross sections are exactly the same as those in Figure 4. Black phase is PI nanodomain. Cylindrical nanodomains are completely reconstructed not only in the  $x$ - $y$  plane but also in other two orthogonal cross sections. Scale bar shows 200 nm. (b) Surface-rendered 3D images obtained from dual-axis tomography, where the PS region has been made transparent. Box size of the 3D image is 250 nm  $\times$  250 nm  $\times$  115 nm.

the dual-axis tomography can provide quantitative 3D data, if the nanostructure is highly anisotropic.

## V. Summary

A three-dimensional (3D) nanostructure of a cylinder forming poly(styrene-*block*-isoprene) (SI) block copolymer was studied by transmission electron microtomography (TEM). In the TEMT experiments one rotates specimens around an axis to obtain a series of tilted projections, which are used to reconstruct 3D structure on the basis of the computerized tomography. Although very powerful, it was found that the TEMT failed to reconstruct part of the cylindrical nanodomains whose orientation had certain angular relationship with the tilt axis (see Figure 4). This is due to an intrinsic and critical problem of the TEMT, called the “missing wedge” problem, that the angular range of the specimen tilt is limited to (at maximum)  $\pm 70^\circ$ . In theory, this limitation leads not only to anisotropic resolution in the resulting 3D reconstruction, i.e., the resolution along the specimen depth is worse than that along the specimen plane, but also to failure in the reconstruction of the nanostructures that fulfill certain angular relationship (see Figure 1). The latter becomes critical in the 3D observation of highly anisotropic nanostructures, such as cylindrical and lamellar nanodomains.

Since the failure in the reconstruction of SI cylindrical nanodomains depended heavily on the orientation of the

nanostructure, a second tilt series in addition to the first one at exactly the same field of view was obtained. The second tilt axis was orthogonal to the first tilt axis. In doing so, since the geometrical relationship of the cylindrical nanodomains and the tilt axis have changed, the cylinders that were not imaged in the first 3D reconstruction appeared in the second reconstruction. The TEMT with two (orthogonal) tilt axes is called "dual-axis TEMT (or dual-axis tomography)", in contrast to the conventional single-axis TEMT (or single-axis tomography). The two sets of 3D reconstruction were found to be complementary. The two 3D reconstructions were then combined in Fourier space to obtain a new 3D reconstruction. The synthesized 3D reconstruction demonstrated that the cylindrical nanodomains, irrespective of their orientation, were successfully captured. Moreover, significant enhancement of image quality was observed in the 3D reconstruction of the dual-axis tomography compared to that of the single-axis tomography. The volume fraction of the PI cylinders,  $f_1$ , evaluated from the dual-axis 3D reconstruction was in excellent agreement with the known volume fraction of the SI copolymer, while  $f_1$  estimated from the single-axis 3D reconstruction was considerably lower than the expected value.

**Acknowledgment.** The authors are grateful to NEDO for supporting this study through a Japanese National Project "Nano Structured Polymer Project" by the Ministry of Economy, Trade and Industry. The authors are grateful to Dr. Y. Nishikawa and Mr. T. Kaneko for their help in the dual-axis TEMT experiments and their analysis.

## Appendix. A Coordinate Transformation in Fourier Space

In this section, a relationship between the Fourier space of reconstruction 2 before and after the coordinate transformation described by eq 1 is discussed. The Fourier spectrum of reconstruction 2 before the coordinate transformation,  $F_2'(\mathbf{q}_2)$ , is given as

$$F_2'(\mathbf{q}_2) = \int f_2'(\mathbf{x}_2) e^{-i\mathbf{q}_2 \cdot \mathbf{x}_2} d\mathbf{x}_2 \quad (\text{A.1})$$

where  $\mathbf{q}_2$ ,  $\mathbf{x}_2$ , and  $f_2'(\mathbf{x}_2)$  are respectively the coordinate in Fourier space, the coordinate in real space, and the real space image of reconstruction 2 before the coordinate transformation. Similarly, the Fourier spectrum after the coordinate transformation,  $F_2(\mathbf{q}_1)$ , is expressed as

$$F_2(\mathbf{q}_1) = \int f_2(\mathbf{x}_1) e^{-i\mathbf{q}_1 \cdot \mathbf{x}_1} d\mathbf{x}_1 \quad (\text{A.2})$$

$\mathbf{q}_1$ ,  $\mathbf{x}_1$ , and  $f_2(\mathbf{x}_1)$  are the same kinds as above after the coordinate transformation.

Substituting eq 1 for eq A.2 gives

$$F_2(\mathbf{q}_1) = \int f_2(\mathbf{A}\mathbf{x}_2 + \mathbf{b}) e^{-i\mathbf{q}_1 \cdot (\mathbf{A}\mathbf{x}_2 + \mathbf{b})} |\mathbf{A}| d\mathbf{x}_2 \quad (\text{A.3})$$

Here  $|\mathbf{A}|$  is the Jacobian, which is introduced by replacing the  $\mathbf{x}_1$  into  $\mathbf{x}_2$ . Since the translation vector  $\mathbf{b}$  affects only on a phase shift in  $F_2(\mathbf{q}_1)$ , one can neglect  $\mathbf{b}$  without loss of generality. Then, eq A.3 becomes

$$F_2(\mathbf{q}_1) = \int f_2(\mathbf{A}\mathbf{x}_2) e^{-i\mathbf{q}_1 \cdot \mathbf{A}\mathbf{x}_2} |\mathbf{A}| d\mathbf{x}_2 \quad (\text{A.4})$$

Note here that, in eq A.4, the integration is carried out

over  $\mathbf{x}_2$ . This means that image intensity of reconstruction 2 at certain  $\mathbf{x}_2$  is required in this calculation. Instead of looking for the image intensity after the coordinate transformation, i.e.,  $f_2(\mathbf{A}\mathbf{x}_2)$ , one can directly obtain the image intensity from  $f_2'(\mathbf{x}_2)$  knowing the relationship between the two coordinates through eq 1. In addition, since an inner product of vectors is equivalent to the matrix product of transposed vector,  $\mathbf{a} \cdot \mathbf{b} = {}^t\mathbf{a}\mathbf{b}$ . Then, eq A.4 can be rewritten as

$$F_2(\mathbf{q}_1) = \int f_2'(\mathbf{x}_2) e^{-i({}^t\mathbf{q}_1\mathbf{A})\mathbf{x}_2} |\mathbf{A}| d\mathbf{x}_2 \quad (\text{A.5})$$

where superscript  $t$  designates the transpose operation. Changing the order of calculation in  $({}^t\mathbf{q}_1\mathbf{A})\mathbf{x}_2$  to  $({}^t\mathbf{q}_1\mathbf{A})\mathbf{x}_2$ , and then reverting the transpose operation to the inner product again, eq A.5 becomes

$$F_2(\mathbf{q}_1) = \int f_2'(\mathbf{x}_2) e^{-i({}^t\mathbf{q}_1\mathbf{A})\mathbf{x}_2} |\mathbf{A}| d\mathbf{x}_2 = F_2'(\mathbf{q}_1{}^t\mathbf{A}) \quad (\text{A.6})$$

By comparing the exponent of eq A.6 with that of eq A.1, one can find a simple relationship,  $\mathbf{q}_2 = \mathbf{q}_1{}^t\mathbf{A}$ .

## References and Notes

- Thurn-Albrecht, T.; Schotter, J.; Kästle, G. A.; Emley, N.; Shibauchi, T.; Krusin-Elbaum, L.; Guarini, K.; Black, C. T.; Tuominen, M. T.; Russell, T. P. *Science* **2000**, *290*, 2126–2129.
- Park, M.; Harrison, C.; Chaikin, P. M.; Register, R. A.; Adamso, D. H. *Science* **1997**, *276*, 1401–1404.
- Hamley, I. W. *Nanotechnology* **2003**, *14*, R39–R54.
- Spontak, R. J.; Patel, N. P. In *Phase Behavior of Block Copolymers*; Hamley, I. W., Ed.; John Wiley & Sons Ltd.: Chichester, 2004.
- Guarini, K. W.; Black, C. T.; Zhang, Y.; Kim, H.; Sikorski, E. M.; Babich, I. V. *J. Vac. Sci. Technol. B* **2002**, *20*, 2788–2792.
- Liu, G.; Ding, J.; Stewart, S. *Angew. Chem., Int. Ed.* **1999**, *38*, 835–838.
- Ro, H. K.; Kim, K. J.; Theato, P.; Gidley, D. W.; Yoon, D. Y. *Macromolecules* **2005**, *38*, 1031–1034.
- Frank, J. In *Principles of Electron Tomography*; Frank, J., Ed.; Plenum Press: New York, 1992.
- Spontak, R. J.; Williams, M. C.; Agard, D. A. *Polymer* **1988**, *29*, 387–395.
- Radzilowski, L. H.; Carragher, B. O.; Stupp, S. I. *Macromolecules* **1997**, *30*, 2110–2119.
- Jinnai, H.; Nishikawa, Y.; Spontak, R. J.; Smith, S. D.; Agard, D. A.; Hashimoto, T. *Phys. Rev. Lett.* **2000**, *84*, 518–521.
- Yamauchi, K.; Takahashi, K.; Hasegawa, H.; Iatrou, H.; Hadjichristidis, N.; Kaneko, T.; Nishikawa, Y.; Jinnai, H.; Matsui, T.; Nishioka, H.; Shimizu, M.; Furukawa, H. *Macromolecules* **2003**, *36*, 6962–6966.
- Wilder, E. A.; Braunfeld, M. B.; Jinnai, H.; Hall, C. K.; Agard, D. A.; Spontak, R. J. *J. Phys. Chem. B* **2003**, *107*, 11633–11642.
- Jinnai, H.; Nishikawa, Y.; Ikehara, T.; Nishi, T. *Adv. Polym. Sci.* **2004**, *170*, 115–167.
- Niihara, K.; Nishikawa, Y.; Nishi, T.; Jinnai, H. *Trans. Mater. Res. Soc. Jpn.*, in press.
- Nishioka, H.; Niihara, K.; Kaneko, T.; Nishikawa, Y.; Yamanaka, J.; Inoue, T.; Nishi, T.; Jinnai, H. *Compos. Interfaces*, in press.
- Jinnai, H.; Shinbori, Y.; Akutagawa, K.; Nishikawa, Y.; Mashita, N.; Nishi, T. *Macromolecules*, submitted for publication.
- Midgley, P. A.; Weyland, M. *Ultramicroscopy* **2003**, *96*, 413–431.
- Radermacher, M.; Hoppe, W. Properties of 3-D reconstruction from Projections by Conical Tilting Compared to Single-Axis Tilting. In *Electron Microscopy 1980*; Brederoo, P., Boon, G., Eds.; Seventh European Congress on Electron Microscopy Foundation: Leiden, 1980.
- Crowther, R. A.; DeRosier, D. J.; Klug, A. *Proc. R. Soc. London* **1970**, *A317*, 319–340.
- Gilbert, P. F. C. *Proc. R. Soc. London* **1972**, *B182*, 89–102.



- (22) Hounsfield, G. N. *A Method and Apparatus for Examination of a Body by Radiation such as X or Gamma Radiation*; The Patent Office: London, England, 1972.
- (23) Penkzek, P.; Marko, M.; Buttle, K.; Frank, J. *Ultramicroscopy* **1995**, *60*, 393–410.
- (24) Mastronarde, D. N. *J. Struct. Biol.* **1997**, *120*, 343–352.
- (25) Spontak, R. J.; Fung, J. C.; Braunfeld, M. B.; Sedat, J. W.; Agard, D. A.; Kane, L.; Smith, S. D.; Satkowski, M. M.; Ashraf, A.; Hadjuk, D. A.; Gruner, S. M. *Macromolecules* **1996**, *29*, 4494–4507.
- (26) Belmont, A. S.; Sedat, J. W.; Agard, D. A. *J. Cell. Biol.* **1987**, *105*, 77–92.
- (27) Lorensen, W. E.; Cline, H. E. *Computer Graphics, SIG-GRAPH '87* **1987**, *21*, 163–169.

MA051705U